

The role of prenucleation clusters in surface-induced calcium phosphate crystallization

Archan Dey¹, Paul H. H. Bomans¹, Frank A. Müller², Julia Will³, Peter M. Frederik¹, Gijbertus de With¹ and Nico A. J. M. Sommerdijk¹*

Unravelling the processes of calcium phosphate formation^{1–4} is important in our understanding of both bone and tooth formation^{5–7}, and also of pathological mineralization, for example in cardiovascular disease^{8–10}. Serum is a metastable solution from which calcium phosphate precipitates in the presence of calcifiable templates such as collagen, elastin and cell debris^{11,12}. A pathological deficiency of inhibitors leads to the uncontrolled deposition of calcium phosphate. In bone and teeth the formation of apatite crystals is preceded by an amorphous calcium phosphate (ACP) precursor phase^{13,14}. ACP formation is thought to proceed through prenucleation clusters—stable clusters that are present in solution already before nucleation—as was recently demonstrated for CaCO_3 (refs 15,16). However, the role of such nanometre-sized clusters as building blocks² for ACP has been debated for many years. Here we demonstrate that the surface-induced formation of apatite from simulated body fluid^{17,18} starts with the aggregation of prenucleation clusters leading to the nucleation of ACP before the development of oriented apatite crystals.

Calcium phosphate is the biomineral most relevant for our day-to-day lives, as it forms the main constituent of bone and teeth^{5–7}. Calcium phosphate deposition also plays an important role in several pathological situations, such as arteriosclerosis^{8–12}. Only recently it was demonstrated that in zebra fish bone¹⁴, as well as in enamel¹³, apatite formation does not occur directly by the association of ions from solution but proceeds through an amorphous calcium phosphate (ACP) precursor phase, even though the generality of this pathway is still under debate¹⁹. Not only did this trigger us to investigate the mechanism of surface-induced mineral deposition from serum, it also urged us to revisit the postulate that ACP consists of subnanometre clusters with a chemical composition $\text{Ca}_9(\text{PO}_4)_6$, the basic unit of the final apatite crystals². Calcium phosphate formation has been proposed to proceed through a cluster-growth model³, but as such nanometre-sized building blocks are difficult to visualize and cannot be described by classical nucleation theory^{20–22} they have been a matter of debate for many years.

As mineralization processes are difficult to investigate at nanometre detail *in vivo*, we employ a model system that we can study with cryogenic transmission electron microscopy (cryoTEM). The application of high-resolution cryoTEM in combination with low-dose selected-area electron diffraction has been instrumental in the visualization of the prenucleation clusters of CaCO_3 (ref. 16). Here we use simulated body fluid (SBF), a solution containing near-physiological concentrations of the most important inorganic

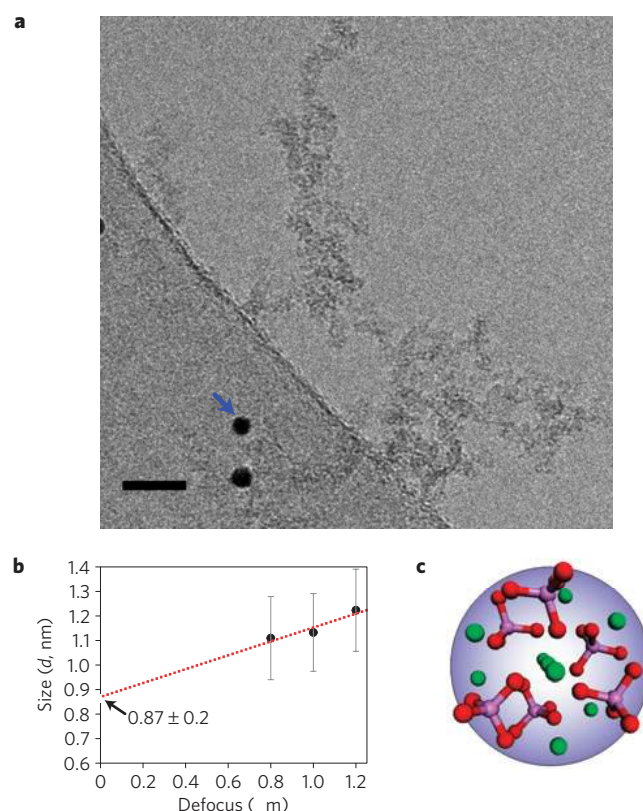


Figure 1 | Stable prenucleation clusters in SBF. a, High-resolution cryoTEM image of assemblies of clusters in SBF kept at 37 °C for 24 h; the arrow indicates gold particles used as a fiducial marker for tomography. Scale bar, 20 nm. **b**, Determination of the true diameter of prenucleation clusters by extrapolation of the diameter measured in HR-cryo TEM images recorded at different defocus values; error bars indicate the standard deviation. **c**, Computer representation of the Posner cluster with composition $\text{Ca}_9(\text{PO}_4)_6$ and a diameter of ~ 0.95 nm.

components in serum, as the mineral source. Through its composition, SBF under physiological conditions is stabilized against precipitation in the absence of a nucleation-inducing surface. In our model a Langmuir monolayer of arachidic acid mimics the biological calcifiable surfaces that induce calcium phosphate nucleation *in vivo*.

¹Laboratory of Materials and Interface Chemistry and Soft Matter CryoTEM Unit, Eindhoven University of Technology, PO Box 513, 5600 MB Eindhoven, The Netherlands, ²Institute of Materials Science and Technology (IMT), Friedrich-Schiller-University of Jena, Loebdergraben 32, D-07743 Jena, Germany, ³University of Erlangen-Nuernberg, Department of Materials Science (Glass and Ceramics), Martensstr. 5, 91058 Erlangen, Germany.

*e-mail: n.sommerdijk@tue.nl.

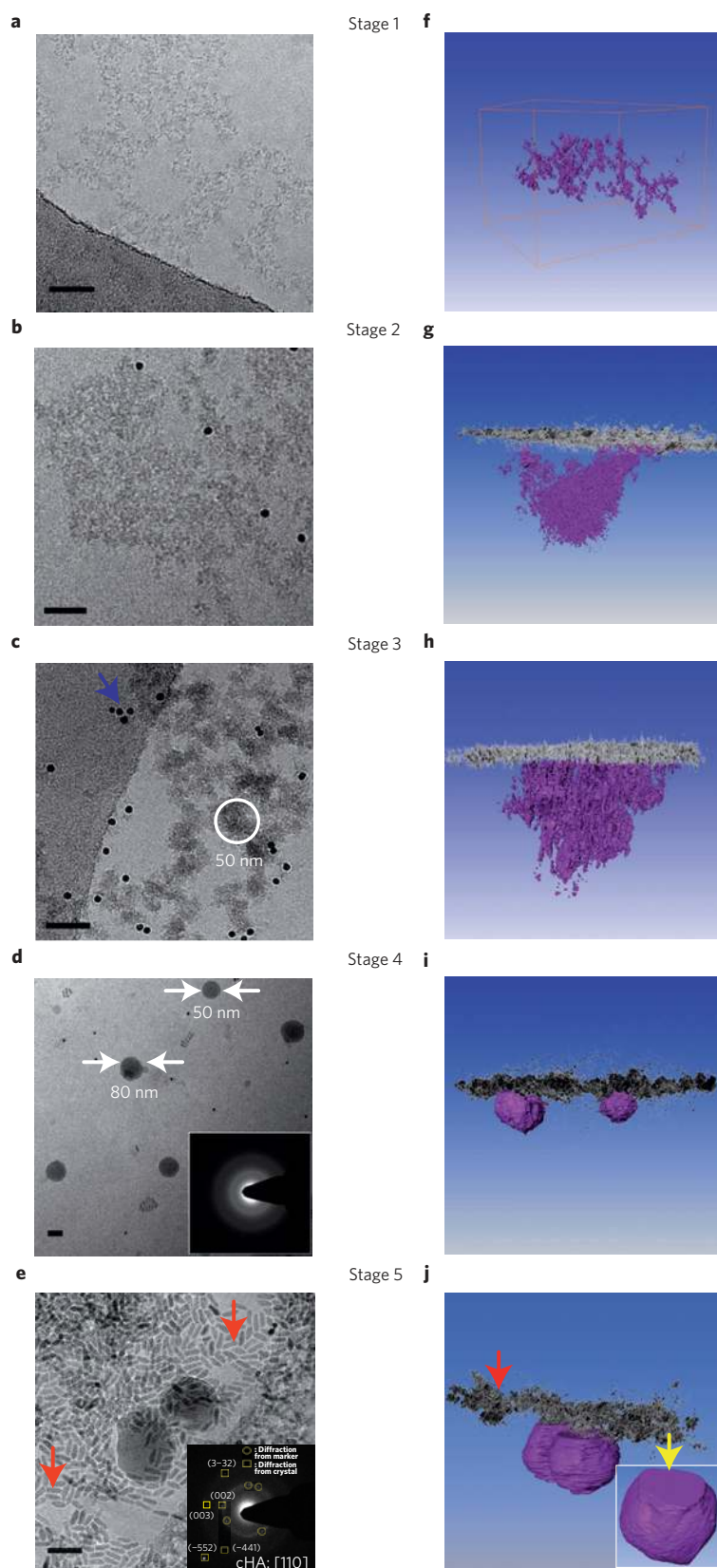


Figure 2 | CryoTEM imaging of different stages of the mineralization process. **a–e**, Two-dimensional projection images; **f–j**, computer-aided three-dimensional visualizations of tomograms; **a,f**, stage 1, the control experiment in the absence of a monolayer; **b,g**, stage 2; **c,h**, stage 3; **d,i**, stage 4; the inset SAED in **d** shows that the spherical particles attached to the monolayer are amorphous; **e,j**, stage 5; the inset SAED in **e** can be indexed as cHA with a [110] zone axis. The preferred nucleating face is (110), indicated by the yellow arrow in the inset of **j**. Please note that for clarity (markers obscuring the image) we have not used the same area for two- and three-dimensional images except in **e,j**. Markers and gold beads are indicated by red and blue arrows, respectively. Scale bars, 50 nm.

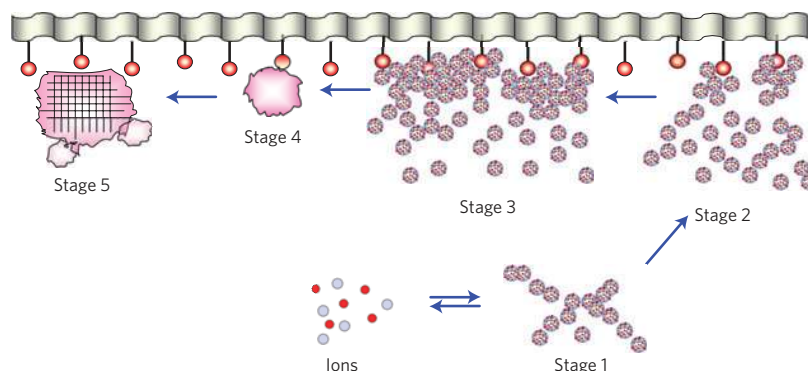


Figure 3 | Schematic representation of the different stages of surface-directed mineralization of calcium phosphate from SBF at 37 °C. Stage 1: loose aggregation of pre-nucleation clusters in equilibrium with ions in solution. Stage 2: pre-nucleation clusters aggregate in the presence of the monolayer with loose aggregates still present in solution. Stage 3: aggregation leads to densification near the monolayer. Stage 4: nucleation of amorphous spherical particles only at the monolayer surface. Stage 5: development of crystallinity following the oriented nucleation directed by the monolayer.

With this system we demonstrate conclusively that crystal nucleation starts with the generation of aggregates of calcium phosphate pre-nucleation clusters that densify at a templating surface. In a next step the densification of these clusters leads to the formation of an amorphous precursor phase which ultimately transforms into the crystalline apatite, of which the orientation of the *c* axis is directed along the nucleation surface.

When prepared at physiological temperature (37 °C) this system produced mineral deposits exclusively at the air–water interface, that is, at the location of the arachidic acid monolayer (Supplementary Fig. S1). After 24 h these deposits were isolated and demonstrated to consist of preferentially oriented nanocrystallites of carbonated hydroxyapatite (cHA) elongated along their crystallographic *c* axis (Supplementary Fig. S2). Subsequently, plunge-freeze vitrification of the mineralizing monolayer at various points in time was used to trap the early stages of the reaction and to monitor the development of the mineral phase in its native hydrated state with cryoTEM (refs 16,23).

High-resolution cryoTEM demonstrated that at 25 °C and in the absence of a monolayer the SBF solution contained isolated nanometre-sized pre-nucleation clusters (Supplementary Fig. S4). After increasing the temperature to 37 °C these clusters were present partially as individual entities or as small aggregates (Fig. 1a), but mainly as loosely aggregated networks within the bulk solution (Fig. 2, stage 1). Size analysis (Fig. 1b) of the observed clusters showed an average diameter of 0.87 ± 0.2 nm, in line with previously reported cluster sizes (0.70–1.00 nm; ref. 3) and the theoretical size of Posner's clusters (0.95 nm; Fig. 1c; ref. 2).

CryoTEM further revealed that the application of the arachidic acid monolayer induced the formation of densified domains within the aggregates of clusters. Cryo-electron tomography (cryoET) demonstrated that this densification only occurs where the cluster aggregates are in contact with the monolayer surface (Fig. 2, stage 2). In time this densification progresses to form spherical domains of ~50 nm size (Fig. 2, stage 3). In a subsequent step these domains transform into dense spherical particles with diameters of 40–80 nm. These nanoparticles were demonstrated to consist of ACP by low-dose selected-area electron diffraction and cryogenic electron-dispersive X-ray spectroscopy (Fig. 2, stage 4, Supplementary Fig. S5). After 12 h, these particles have developed into spheroidal crystals with an average diameter of 120 nm (Fig. 2, stage 5). As expected for mineral deposits from SBF (ref. 18) and in line with their spheroidal morphology²⁴, low-dose selected-area electron diffraction identified these crystals as B-type cHA—apatite in which some of the phosphate groups are substituted with carbonate ions from the SBF solution²⁵. The diffraction patterns were indexed with a zone axis implying that the presence of the

monolayer leads to a preferred nucleation of the (110) face. This agrees well with previous reports of the formation of apatite crystals preferentially oriented with their *c* axis parallel to the surface of a Langmuir–Blodgett film²⁶.

CryoET revealed that for all these crystals the nucleation plane forms a flat patch with which they interact with the orientation-directing monolayer. The (110) face is a polar surface in which the Ca^{+2} ions form a rectangular unit cell with dimensions of $5.44 \text{ \AA} \times 3.46 \text{ \AA}$ (Supplementary Fig. S6). Although the dimensions of two of such cells are in reasonable agreement with the lattice of arachidic acid on a calcium-containing monolayer ($7.57 \text{ \AA} \times 4.93 \text{ \AA}$; ref. 27), currently there is no information that supports a true epitaxial relation between the organic and inorganic phases.

In later stages of the mineralization reaction we only observed crystalline particles (stage 5), coexisting with a remaining small number of ~50 nm ACP nanoparticles (stage 4, Supplementary Fig. S7). This suggests that the ACP nanoparticles have maximum stability at this diameter, similar to what was previously observed for nanoparticles of diffraction-amorphous CaCO_3 , which, depending on the procedures used, have a preferred diameter of 30–50 nm (refs 16,23). The crystals were never observed together with aggregates of clusters (stage 1–3) or intermediates. This is in contrast to the earlier time points where stages 1–4 (Fig. 2) could all be encountered in the same sample. However, even for these early points stages 3 and 4 were never localized in the same area, suggesting that the transition between these two phases is a fast, concerted process.

Mineral formation from SBF in the above experiments occurs exclusively through heterogeneous nucleation at the surface of the monolayer. This is in clear contrast to the recently reported formation of CaCO_3 from an fast out-gassing $\text{Ca}(\text{HCO}_3)_2$ solution in the presence of a stearic acid monolayer¹⁶. In that case, the aggregation of pre-nucleation clusters led to the homogeneous nucleation of amorphous nanoparticles in solution, despite the presence of the organic template. As a recent theoretical study predicted the stabilization of the pre-nucleation clusters by foreign ions such as Na^+ (ref. 28), we attribute the absence of homogeneous nucleation of ACP in bulk solution to the relatively high concentration of Na^+ , Mg^{2+} , Cl^- and HCO_3^- ions in SBF (ref. 29). Indeed, cryoET showed that in the presence of an arachidic monolayer a subphase consisting of a Tris-buffered (pH 7.4) solution containing only 2.5 mM CaCl_2 and 1.0 mM K_2HPO_4 already after 1 h produced diffraction-amorphous nanoparticles with diameters of 30–80 nm in the bulk solution (Supplementary Fig. S8). Hence, we assign the difference in nucleation behaviour—heterogeneous versus homogeneous nucleation—to the higher driving force for homogeneous nucleation in the calcium carbonate and Tris-buffered CaCl_2 and K_2HPO_4 . The reduced kinetics in SBF

also underlines the higher level of control over the localization of mineral deposition under physiological conditions.

The above observations clearly show that the formation of apatite crystals from SBF at physiological temperature in the presence of an arachidic acid monolayer proceeds through a multistage process (Fig. 3) that involves the formation and aggregation of prenucleation clusters. In contrast to our recent reports on the template-directed growth of calcium carbonate¹⁶, and the mineralization of collagen³⁰, the present study enables us to distinguish the different stages before the nucleation of the amorphous phase. In the first stage the prenucleation clusters, present in the SBF, aggregate to form free-floating, loosely associated networks that are stable in solution. In the second stage parts of the cluster aggregates that are in contact with the organic film start to densify by adapting a closer packing of the clusters. The continuation of this densification process leads to defined domains of closely associated clusters with diameters of ~50 nm (stage 3) attached to the monolayer, which further fuse to form monolayer-suspended ACP particles. These nanoparticles further grow and develop crystallinity, yielding spheroid crystals of B-type cHA. The development of crystallinity is guided by the monolayer as shown by the alignment of the crystallographic *c* axis along the nucleating surface, following specific nucleation from the (110) face. The spheroidal morphology of cHA is typical for crystals grown in the presence of higher carbonate concentrations²⁴. The more typical plate-like morphology of the final apatite crystals (Supplementary Fig. S2b) is most probably due to a gradual decrease of the carbonate in the SBF solution by consumption of the ions during the reaction and out-gassing of CO₂ during the course of the experiment.

Our experiments not only confirm the existence of nanometre-sized prenucleation clusters in SBF solutions, they also show their role as building blocks in the formation of ACP. The observed ordering of prenucleation clusters at the templating surface also supports the previously advocated cluster growth process³. However, the process does not lead to the direct crystallization of apatite, but to the nucleation of ACP that only later transforms into a crystalline phase, most likely through a solid-state transition^{7,31}. In contrast to what was found in bone³², we did not observe octacalcium phosphate as an intermediate phase.

Indirectly, our studies also support the original proposition of Posner *et al.*² that ACP is formed from such clusters, although their composition may be different from the stabilized clusters present in solution. In fact, we propose that the presence of the nucleating surface induces structural and compositional changes that enable the denser packing of the clusters and their subsequent fusion to form ACP. However, at present there is no information concerning the structural stability of the clusters throughout the different steps, nor on the detailed mechanism of the cluster aggregate-to-ACP transition.

The discussion of the relevance of *in vitro* models for understanding selected aspects of *in vivo* systems has always been inherent to their use. Although the application of SBF to predict the *in vivo* bioactivity of implants has been a subject of discussion³³, in the present work the use of SBF enables us to study exclusively the effect of the nucleating surface on calcium phosphate mineralization, without interference of bulk precipitation or the effect of additives. Moreover, with our model system that focuses on unravelling the mechanism of mineral formation rather than on mimicking the biological environment, we are indeed able to visualize all stages from the prenucleation clusters to the formation of cHA on a nucleating surface.

By confirming and integrating the finding of prenucleation clusters in calcium phosphate solutions as well as the previously proposed cluster growth model with the ACP-mediated apatite formation, our results provide an integral and comprehensive model for surface-controlled apatite formation with implications

for our understanding and possibly for the treatment of pathological mineral formation in biological environments.

Methods

CryoTEM and cryoET. For the preparation of cryoTEM samples from monolayers with attached mineralization solution we made use of a vitrification robot (FEI Vitrobot Mark III) equipped with a humidity- and temperature-controlled glove box (see details in Methods and Supplementary Fig. S3). Using this approach we can load the whole mineralization system onto a holey carbon-coated cryoTEM grid with minimal disturbance of the system, while maintaining 100% humidity and a constant temperature of 37 °C (refs 16,23).

CryoTEM grids, R2/2 Quantifoil Jena grids, were purchased from Quantifoil Micro Tools GmbH. Before the vitrification procedure the grids were surface plasma treated using a Cressington 208 carbon coater. The cryoTEM experiments were carried out on a FEI Technai 20 (type Sphera) TEM or on the TU/e CryoTitan (FEI) (www.cryotem.nl). For the Technai 20 a Gatan cryo-holder operating at about -170 °C was used. The Technai 20 is equipped with a LaB₆ filament operating at 200 kV and the images were recorded using a 1 k × 1 k Gatan CCD (charge-coupled device) camera. The TU/e CryoTitan is equipped with a field emission gun operating at 300 kV and with a postcolumn Gatan energy filter. Images were recorded using a 2 k × 2 k Gatan CCD camera. The three-dimensional reconstructions were carried out with the software Inspect 3D v.3.0 (FEI Company). For the segmentation and visualization of the three-dimensional volume, Amira 4.1.0 (Mercury Computer Systems) was used. The DiffTools package³⁴ supported by DigitalMicrograph software was used as an aid to analyse the diffraction patterns and crystallography data from the Inorganic Crystal Structure Database (cHA: 93783; ref. 25) were used for indexing the diffraction patterns.

Experimental protocol for cryoTEM sample preparation. As a model system, we used a monolayer of arachidic acid [CH₃(CH₂)₁₈COOH] as the nucleation surface, spread on SBF (Supplementary Fig. S1a). The mineralization reaction then proceeds by heating up the system to 37 °C. Specimens were prepared at different time points by draining the solution and loading the monolayer with calcium phosphate particles on the cryoTEM grid, in a glove box in which the temperature and the humidity were controlled at 37 °C and 100% relative humidity. At the beginning of the reaction the cryoTEM grids were present in the solution, on a metallic support. The cryoTEM grids are 200 mesh copper grids, covered by a carbon film that contained a regular pattern of 2 µm holes in the carbon layer (Supplementary Fig. S3, step 1). After a certain reaction time the SBF was drained and the monolayer with calcium phosphate particles loaded onto these cryoTEM grids with minimal disturbance of the system (step 2). The grid was transferred to a fully automated vitrification robot (Vitrobot). The environmental conditions were kept constant at 37 °C and 100% relative humidity. A suspension of 3 µl of 4.96 × 10⁻⁵ mM of CdSe nanorod solution in CHCl₃ was added on the hydrophobic side of the monolayer (step 3) to mark the monolayer and 3 µl of a 6 nm gold solution was also added from the opposite side of the grid for reconstruction of the tomography tilt series. Finally, excess of liquid was removed by automatic blotting to produce a thin liquid layer (around 100 nm thick) containing the monolayer and the calcium phosphate particles, and the reaction was quenched by plunging the grid into melting ethane (step 4). For all crystallization experiments, SBF-10¹⁸ (see the ion concentration in Supplementary Table S1) was used. The required salts were purchased from Merck, purity ≥99%, the arachidic acid from Aldrich, purity ≥99.5%, and the chloroform from Biosolve, purity >99.9%. Hydrophobic CdSe nanorods were provided by Patrick Chin (TU/e, Eindhoven). The monolayers were prepared by spreading a CHCl₃ solution of arachidic acid (1 mM). The amount of arachidic acid has been calculated to cover the surface with a close-packed organization.

Received 12 March 2010; accepted 14 October 2010;
published online 14 November 2010

References

- Brechevic, L. J. & Furedi-Milhofer, H. Precipitation of calcium phosphates from electrolyte solutions. II. The formation and transformation of precipitates. *Calif. Tissue Res.* **10**, 82–90 (1972).
- Posner, A. S. & Betts, F. Synthetic amorphous calcium phosphate and its relation to bone mineral structure. *Acc. Chem. Res.* **8**, 273–281 (1975).
- Onuma, K. & Ito, A. Cluster growth model for hydroxyapatite. *Chem. Mater.* **10**, 3346–3351 (1998).
- Müller, F. A., Müller, L., Caillard, D. & Conforto, E. Preferred growth orientation of biomimetic apatite crystals. *J. Cryst. Growth* **304**, 464–471 (2007).
- Brown, W. E. & Chow, L. C. Chemical properties of bone mineral. *Annu. Rev. Mater. Sci.* **6**, 213–236 (1976).
- Smith, C. E. Cellular and chemical events during enamel maturation. *Crit. Rev. Oral Biol. Med.* **9**, 128–161 (1998).
- Olszta, M. J. *et al.* Bone structure and formation: A new perspective. *Mater. Sci. Eng. R* **58**, 77–116 (2007).
- Luo, G. *et al.* Spontaneous calcification of arteries and cartilage in mice lacking matrix GLA protein. *Nature* **386**, 78–81 (1997).

9. Hui, M., Li, S. Q., Holmyard, D. & Cheng, P. T. Stable transfection of nonosteogenic cell lines with tissue nonspecific alkaline phosphatase enhances mineral deposition both in the presence and absence of β -glycerophosphate: Possible role for alkaline phosphatase in pathological mineralisation. *Calcif. Tissue Int.* **60**, 467–472 (1997).
10. Dorozhkin, S. V. & Epple, M. Biological and medical significance of calcium phosphates. *Angew. Chem. Int. Ed.* **41**, 3130–3146 (2002).
11. Urry, D. W. Molecular basis for vascular calcification. *Perspect. Biol. Med.* **17**, 68–84 (1974).
12. Westenfeld, R. *et al.* Fetuin-A protects against atherosclerotic calcification in CKD. *J. Am. Soc. Nephrol.* **20**, 1264–1274 (2009).
13. Beniash, E., Metzler, R. A., Lam, R. S. K. & Gilbert, P. U. P. A. Transient amorphous calcium phosphate in forming enamel. *J. Struct. Biol.* **166**, 133–143 (2009).
14. Mahamid, J. *et al.* Mapping amorphous calcium phosphate transformation into crystalline mineral from the cell to the bone in zebrafish fin rays. *Proc. Natl Acad. Sci. USA* **107**, 6316–6321 (2010).
15. Gebauer, D., Volkel, A. & Colfen, H. Stable prenucleation calcium carbonate clusters. *Science* **322**, 1819–1822 (2008).
16. Pouget, E. M. *et al.* The initial stages of template-controlled CaCO_3 formation revealed by cryo-TEM. *Science* **323**, 1455–1458 (2009).
17. Ayako, O. *et al.* Preparation and assessment of revised simulated body fluids. *J. Biomed. Mater. Res.* **65A**, 188–195 (2003).
18. Muller, L. & Muller, F. A. Preparation of SBF with different HCO_3^- content and its influence on the composition of biomimetic apatites. *Acta Biomater.* **2**, 181–189 (2006).
19. Rey, C., Combes, C., Drouet, C. & Glimcher, M. Bone mineral: Update on chemical composition and structure. *Osteoporos. Int.* **20**, 1013–1021 (2009).
20. Auer, S. & Frenkel, D. Prediction of absolute crystal-nucleation rate in hard-sphere colloids. *Nature* **409**, 1020–1023 (2001).
21. Wang, L. & Nancollas, G. H. Pathways to biomineralization and biomineralization of calcium phosphates: The thermodynamic and kinetic controls. *Dalton Trans.* 2665–2672 (2009).
22. Erdemir, D., Lee, A. Y. & Myerson, A. S. Nucleation of crystals from solution: Classical and two-step models. *Acc. Chem. Res.* **42**, 621–629 (2009).
23. Pichon, B. P., Bomans, P. H. H., Frederik, P. M. & Sommerdijk, N. A. J. M. A quasi-time-resolved cryoTEM study of the nucleation of CaCO_3 under Langmuir monolayers. *J. Am. Chem. Soc.* **130**, 4034–4040 (2008).
24. Legeros, R. Z., Trautz, O. R., Legeros, J. P., Klein, E. & Shirra, W. P. Apatite crystallites: Effects of carbonate on morphology. *Science* **155**, 1409–1411 (1967).
25. Ivanova, T. I., Frank-Kamenetskaya, O. V., Kol'tsov, A. B. & Ugolkov, V. L. Crystal structure of calcium-deficient carbonated hydroxyapatite. Thermal decomposition. *J. Solid State Chem.* **160**, 340–349 (2001).
26. Sato, K., Kogure, T., Kumagai, Y. & Tanaka, J. Crystal orientation of hydroxyapatite induced by ordered carboxylic groups. *J. Colloid Interface Sci.* **240**, 133–138 (2001).
27. DiMasi, E., Olszta, M. J., Patel, V. M. & Gower, L. B. When is template directed mineralization really template directed? *Cryst. Eng. Comm.* **5**, 346–350 (2003).
28. Xilin, Y. & Malcolm, J. S. Biological calcium phosphates and Posner's cluster. *J. Chem. Phys.* **118**, 3717–3723 (2003).
29. Termine, J. D. & Posner, A. S. Calcium phosphate formation *in vitro*: I. Factors affecting initial phase separation. *Arch. Biochem. Biophys.* **140**, 307–317 (1970).
30. Nudelman, F. *et al.* Collagen can directly control the formation of bone apatite in the presence of a calcium-ion binding polymer in solution. *Nature Mater.* published online doi:10.1038/NMAT2875 (24 October 2010).
31. Tsuji, T., Onuma, K., Yamamoto, A., Iijima, M. & Shiba, K. Direct transformation from amorphous to crystalline calcium phosphate facilitated by motif-programmed artificial proteins. *Proc. Natl Acad. Sci. USA* **105**, 16866–16870 (2008).
32. Crane, N. J., Popescu, V., Morris, M. D., Steenhuis, P. & Ignelzi, J. M. A. Raman spectroscopic evidence for octacalcium phosphate and other transient mineral species deposited during intramembranous mineralization. *Bone* **39**, 434–442 (2006).
33. Bohner, M. & Lemaire, J. Can bioactivity be tested *in vitro* with SBF solution? *Biomaterials* **30**, 2175–2179 (2009).
34. Mitchell, D. R. G. DiffTools: Electron diffraction software tools for digitalmicrograph. *Microsc. Res. Tech.* **71**, 588–593 (2008).

Acknowledgements

Supported by the European Community (project code NMP4-CT-2006-033277) and the Netherlands Organization for Scientific Research (NWO). We are grateful to F. Nudelman for discussions and experimental assistance. We thank E. M. Pouget for her help in experimental design, F. L. Boogaard and J. J. van Rosmalen for their contribution to the three-dimensional reconstructions of the tomograms, M.M.R.M. Hendrix for his help with X-ray diffraction and P. T. K. Chin for providing the CdSe nanorods.

Author contributions

A.D. carried out all experiments and cowrote the manuscript. P.H.H.B. and P.M.F. provided support with the cryoTEM. F.A.M. and J.W. provided SBF. G.W. and N.A.J.M.S. supervised the project and N.A.J.M.S. cowrote the manuscript. All authors discussed the results and revised the manuscript.

Additional information

The authors declare no competing financial interests. Supplementary information accompanies this paper on www.nature.com/naturematerials. Reprints and permissions information is available online at <http://npg.nature.com/reprintsandpermissions>. Correspondence and requests for materials should be addressed to N.A.J.M.S.